Processing of 72-K water-rich ices by keV and MeV oxygen ions: implications for the Saturnian moon Enceladus

M G Rachid, S Pilling, W R M Rocha, A Agnihotri, H Rothard, P Boduch

Processing of 72 K water-rich ices by keV and MeV oxygen ions: Implications for the Saturnian moon Enceladus

M. G. Rachid[1,3], S. Pilling[1], W. R. M. Rocha[1,4], A. Agnihotri[2] , H. Rothard[2], P. Boduch[2]

[1] Universidade do Vale do Paraíba (UNIVAP), Laboratório de Astroquímica e Astrobiologia (LASA), Av. Shishima Hifumi, 2911, Urbanova, CEP: 12244000, São José dos Campos, SP, Brazil

[2] Centre de Recherche sur les Ions, les Matériaux et la Photonique, Normandie Univ, ENSICAEN, UNICAEN, CEA, CNRS, CIMAP, 14000 Caen, France

[3]Current address: Leiden Observatory, Leiden University, PO Box 9513, 2300 RA Leiden, The Netherlands

[4] Niels Bohr Institute & Centre for Star and Planet Formation, University of Copenhagen, *Øster Voldgade 5-7, DK-1350 Copenhagen K., Denmark*

Abstract

The processing of H_2O:CO_2:CH_4 (10:1:1) and H_2O:CO_2:CH_4:NH_3 (10:1:1:1) ices at 72 K by oxygen ions was studied in attempt to simulate the physicochemical effects induced by energetic ions on Enceladus surface (or similar cold surfaces in the outer Solar System). The experiments were carried out at GANIL (*Grand Accélérateur National d'ions Lourds*) in Caen/France. The samples were irradiated with 15.7 MeV O^{5+} at the IRRSUD beamline and with 108 keV O^{6+} at the ARIBE beamline. The frozen samples were monitored by FTIR Spectroscopy (4000 - 650 cm^{-1}, 2.5 - 15.4 μm, at 1 cm^{-1} resolution). The identified molecular species formed during irradiation were: CO, OCN^-, CH_3OH, HCN, CN^-,H_2CO_3, HNCO, HCO and CO_3. The effective formation cross sections for the synthesis of new species and the effective molecular destruction cross sections of the parent species in the experiments with MeV ions were found to be of the order of 10^{-14} - 10^{-13} cm^2. For the keV ions experiments these values were of the order of 10^{-16} - 10^{-15} cm^2. The fluence at which the sample reaches chemical equilibrium and the molecular abundances in this region (Equilibrium branching ratios) were estimated. These experiments suggest that the chemical inventory on Enceladus surface can be influenced by the incidence of charged particles onto the moon's surface.

Keywords: astrochemistry, methods:laboratory:molecular, methods:laboratory:solid state, techniques: spectroscopic

1. Introduction

The Saturnian moons have been pointed out as potential places to support extra-terrestrial life and to host prebiotic molecules (Kazeminejad et al. 2002, Parkinson et al. 2008, Raulin 2008, McKay et al. 2014). Among these moons, Enceladus is one of the most promising targets because it harbors a salty and warm subsurface ocean (Postberg et al. 2009, Thomas et al. 2016). Material from this ocean vents through four fissures, known as tiger stripes, in the south pole of Enceladus from approximately 100 geysers spreading volatiles, organic molecules, salts, and ice grains into space (Postberg et al. 2009, Teolis et al. 2010, Porco et al. 2014). The material erupting from the tiger stripes are the Enceladus plumes, and data from the Cassini mission have revealed that they

contain a rich molecular inventory (Brown et al. 2006, Matson et al. 2007, Waite et al. 2009), that includes macromolecular organics with molecular masses above 200 u (Postberg et al. 2018a).

The Enceladus surface and plumes were extensively investigated during flybys of the Cassini spacecraft using a variety of instruments onboard it. The Cassini's Near Infrared Mass Spectrometer (NIMS) revealed that Enceladus surface is mainly composed of water ice with smaller quantities of volatile species, such as CO_2, NH_3, and tholins (Brown et al. 2006, Hendrix et al. 2010, Combe et al.2019). The moon's surface temperature was mapped using the CIRS instrument (Composite Infrared Spectrometer) and showed a temperature gradient varying from 35 K in the north pole up to 72 K in the equatorial region. Temperatures as high as 170 K were also measured close to the tiger stripes (Spencer et al. 2006).

The surface of Enceladus is recovered by infalling material from the plumes (Southworth et al. 2019) and it is constantly bombarded with ions and electrons from the magnetosphere of Saturn as well as X-rays and UV photons from the Sun. This bombardment can lead to ejection of molecules from the icy surface and the grains floating around Enceladus (sputtering and photo-desorption). Also, this bombardment can trigger the formation of new chemical species on the Enceladus surface and on the icy grains expelled from the plumes.

In this work, we analyzed the effects of medium-mass (e.g. oxygen) ion bombardment in H_2O:CO_2:CH_4(10:1:1) and H_2O:CO_2:CH_4:NH_3(10:1:1:1) ices at 72 K, conditions similar to that Enceladus' surface (Spencer et al. 2006). The choice of medium mass ions relies on the fact that the saturnian inner magnetosphere is mainly populated by water-derived atoms and molecular ions, the so-called water group ions, as O^+, OH^+, H_2O^+, H_3O^+ (Sittler et al. 2005, Young et al. 2005), with kinetic energies peaking at hundreds of keV. The ion irradiation employed oxygen ions of different energies: 108 keV O^{6+} and 15.7 MeV O^{5+}. A work involving the processing of similar ice samples by keV electrons was performed by Bergantini et al. (2014a). Interestingly, the authors reported that some species not yet detected on Enceladus, for example OCN^- and $HCONH_2$, can be formed in conditions similar to those found at the moons' north pole. Since charged particles are also important ionizing agents impinging on Enceladus (and other icy moons), radiolysis experiments can be used along with data from the Cassini spacecraft for a better understanding the chemical complexity of Enceladus and other icy-moons of the outer Solar System.

2. Experimental Methodology

The experiments were performed at the "*Grand Accélérateur National d'Ions Lourds*" (GANIL) in Caen-France. The irradiation with 108 keV O^{6+} ions were performed at the low energy facility ARIBE (*Accélérateurs pour les Recherches avec les Ions de Basses Energies*), and the experiments with the 15.7 MeV O^{5+} ions at the IRRSUD (*IRRadiation SUD*) beamline. The CASIMIR chamber (*Chambre d'Analyse par Spectroscopie Infrarouge des Molécules IRradiées*) was coupled to the different beamlines. The set-up, shown in Fig. 1, consists of a stainless steel chamber at high vacuum (base pressure ~ 2×10^{-7} mbar); a cryostat system that is thermally connected to the sample holder; a CsI substrate where the ices are grown; a pre-chamber for mixing the gases and vapor molecules; and an inlet where the gas mixtures are admitted into the chamber.

The sample-cryostat system can be rotated up to 180° and fixed at three different positions that allow i) the front deposition of gas mixtures onto the substrate; ii) the FTIR measurements in the transmission mode; and iii) the sample irradiation. The gas mixtures were prepared by mixing volumes of gases (or vapors) in the desired ratio. The mixtures were admitted into the chamber through a needle valve and deposited onto the CsI substrate at 12 K. The samples were then heated up to 72 K at a rate of 3 K min^{-1} and kept at this temperature during the irradiation. *In-situ* Fourier-transformed infrared spectra were taken before irradiation and at different fluences with a Nicolet FTIR spectrometer (Magna 550) from 4000 cm^{-1} to 650 cm^{-1} with 1 cm^{-1} resolution. More

details of the experimental setup can be found elsewhere (Duarte et al. 2009, Pilling et al. 2010a, 2010b, Lv et al. 2012).

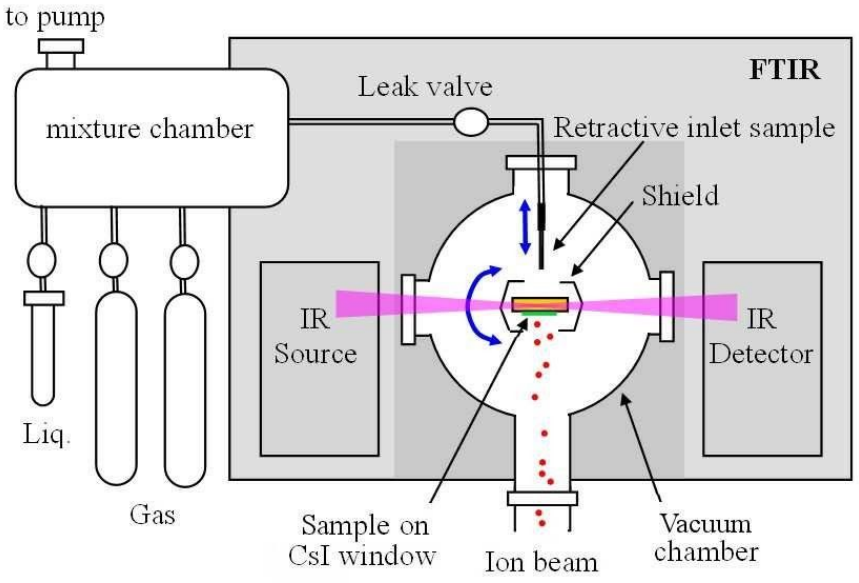

Figure 1: Schematic picture of the experimental apparatus (CASIMIR chamber). The sample holder rotates to three different positions to permit the sample deposition, irradiation, and spectra acquisition (from Pilling et al. 2010a)

The samples were irradiated up to a maximum fluence of about 10^{14} ions cm^{-2}, for the experiments with MeV ions, and 10^{16} ions cm^{-2} for the experiments with keV ions. Table 1 shows the maximum projectile fluences that the ices were exposed during the irradiations.

The molecular column density of the species in the ice is related to the optical depth (τ_ν) and the vibrational mode band strength (A) by (d'Hendecourt and Allamandola 1986):

$$N = \frac{1}{A}\int \tau_\nu d\nu = \frac{2{,}3}{A}\int Abs_\nu d\nu \quad \text{[molecules cm}^{-2}\text{]} \qquad (1)$$

where $\tau_\nu = ln(I_0/I)$, where I_0 and I are the intensity of light at a given frequency before and after passing through a sample, respectively, A is the vibrational mode band strength (in cm molecule^{-1}) and Abs_ν is the absorbance measured by the FTIR at a wavenumber ν ($Abs_\nu = ln\,(I_0/I) / ln(10) = \tau_\nu /2.3$). The initial and final column density of all parent molecules were calculated using Equation 1. In these calculations, we estimated the initial column density as the sum of the initial column density of the parent species (H_2O, CO_2, CH_4 and NH_3). The total column density of the samples are shown in Table 1.

Knowing the molecular column density of all the species in the samples before and after irradiation, it is possible to estimate the ice thickness using the following equation, from Pilling et al. (2011):

$$d = \frac{N}{6.02 \times 10^{23}} \frac{M}{\rho} \times 10^4 \qquad \text{[μm]} \qquad (2)$$

where N is the column density, in units of molecules cm^{-2}, M is the molar mass in units of g mol^{-1}, and ρ is the density in units of g cm^{-3} for the considered species. In Table 1 the thickness of the ice samples is estimated as the sum of the individual components of the sample. The density of each component was assumed to be the same as for pure ices (Brunetto et al. 2008, Satorre et al. 2008): ~1.0 g cm^{-3} for H_2O, 1.8 g cm^{-3} for CO_2, 0.44 g cm^{-3} for CH_4 and 0.8 g cm^{-3} for NH_3 .

Table 1: Summary of the experiments - Experiment label, sample composition, projectile employed in the irradiation, maximum fluence (F_{max}), sum of the column density of the molecules in the non-irradiated ice (N_0) and after maximum fluence (N_f), initial thickness (d_0), and final thickness (d_f). All the ice samples were irradiated at 72 K.

Sample parameters							
Exp. Label	**Sample**	**Projectile**	**F_{max} (ions cm^{-2})**	**N_0 (molec cm^{-2})**	**d_0 (μm)**	**N_f (molec cm^{-2})**	**d_f (μm)**
#SI-1	H_2O:CO_2:CH_4 (10:1:1)	15.7 MeV $^{16}O^{5+}$ (IRRSUD BEAMLINE)	3.0×10^{14}	7.5×10^{18}	2.25	6.3×10^{18}	1.96
#SI-2[a]	H_2O:CO_2:CH_4:NH_3 (10:1:1:1)	15.7 MeV $^{16}O^{5+}$ (IRRSUD BEAMLINE)	1.0×10^{14}	4.5×10^{18}	1.53	3.0×10^{18}	0.94
#LI-1	H_2O:CO_2:CH_4 (10:1:1)	108 keV $^{16}O^{6+}$ (ARIBE BEAMLINE)	1.3×10^{16}	7.8×10^{18}	3.02	7.2×10^{18}	2.25
#LI-2[a]	H_2O:CO_2:CH_4:NH_3 (10:1:1:1)	108 keV $^{16}O^{6+}$ (ARIBE BEAMLINE)	1.2×10^{16}	9.3×10^{18}	3.34	7.9×10^{18}	2.72

[a] Samples with ammonia.

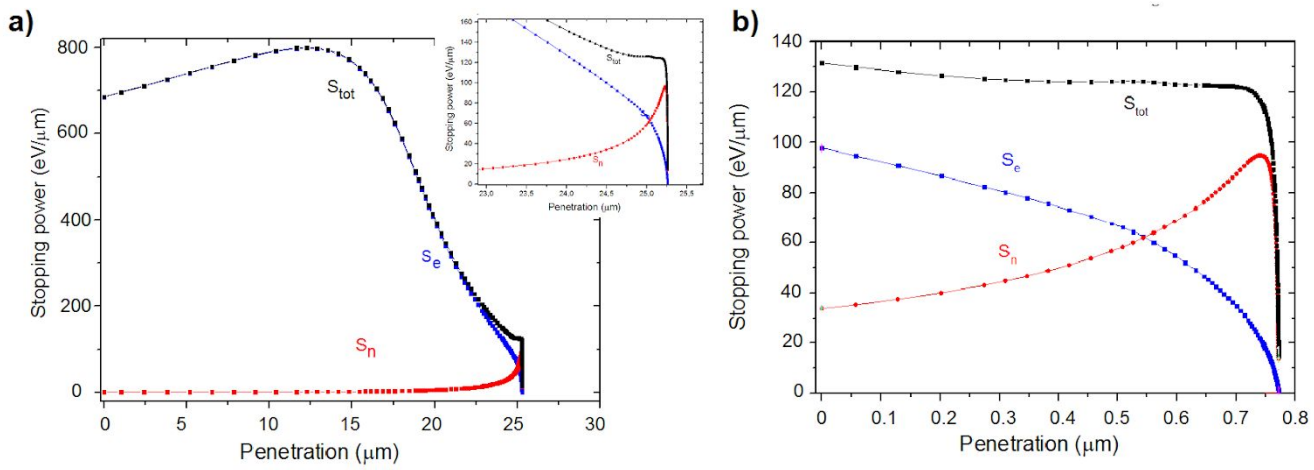

Figure 2: Evolution of the stopping power (deposited energy) as a function of penetration depth of the incoming projectile ions in the samples. a) For experiments #SI-1 and #SI-2 with $^{16}O^{5+}$ 15.7 MeV ions at the IRRSUD beamline. The inset shows the region close to the complete stopping (implantation) of 15.7 MeV ions in the sample. b) For experiments #LI-1 and #LI-2 with 108 keV ions at ARIBE beamline. The calculations were performed with the SRIM code (Ziegler et al. 2010).

The stopping power and the penetration depth of the incoming ions in samples with compositions similar to the ones studied here were calculated using the software SRIM (Ziegler et al. 2010). The stopping power (deposited energy) plotted as a function of the penetration depth of the projectiles is shown in Figure 2. From panel a (Figure 2) it is possible to see that the energy loss of the MeV ions inside the sample happens mainly by electronic interactions (inelastic interactions) with the atoms of the target material. For the keV ions, the energy loss is both by interaction with electrons and nucleus (elastic interactions) of the target material. These two ways of energy transfer can result in different induced chemistry within the ice samples. Using the stopping power calculated by SRIM it is possible to calculate the way in which energy was transferred to the target material.

The maximum penetration depth of the oxygen ions is around 25 μm for the 15.7 MeV oxygen ions and around 0.7 μm for the 108 keV oxygen ions. Considering the initial sample thickness (listed in Table 1), the MeV ions cross the entire length of the sample, processing the surface as well as the ice bulk. In contrast, the 100 keV ions are implanted in the sample,

processing just a portion of the ices. This also implies a relatively smaller yield of molecular fragments from radiolysis by the latter when compared to MeV projectiles. The effects of the implantation of oxygen projectiles in the ices (i.e. the contribution of this atom in the chemical synthesis of new species) were not analyzed in this work since we cannot distinguish between implanted oxygen projectiles and the oxygen atoms from the H_2O and CO_2 molecules originally in the sample.

3. Results

The IR spectra of the non-irradiated and irradiated samples (at maximum fluence) for all the experiments are shown in Figures 3, 4, 5 and 6. In the irradiated spectra (black full lines in the figures), new infrared features, associated with new molecular species, are presented. Some bands from parent and daughter species are indicated in the figures. All the spectra were baseline corrected using a spline fit tool available in the software, Origin, and offset for better visualization.

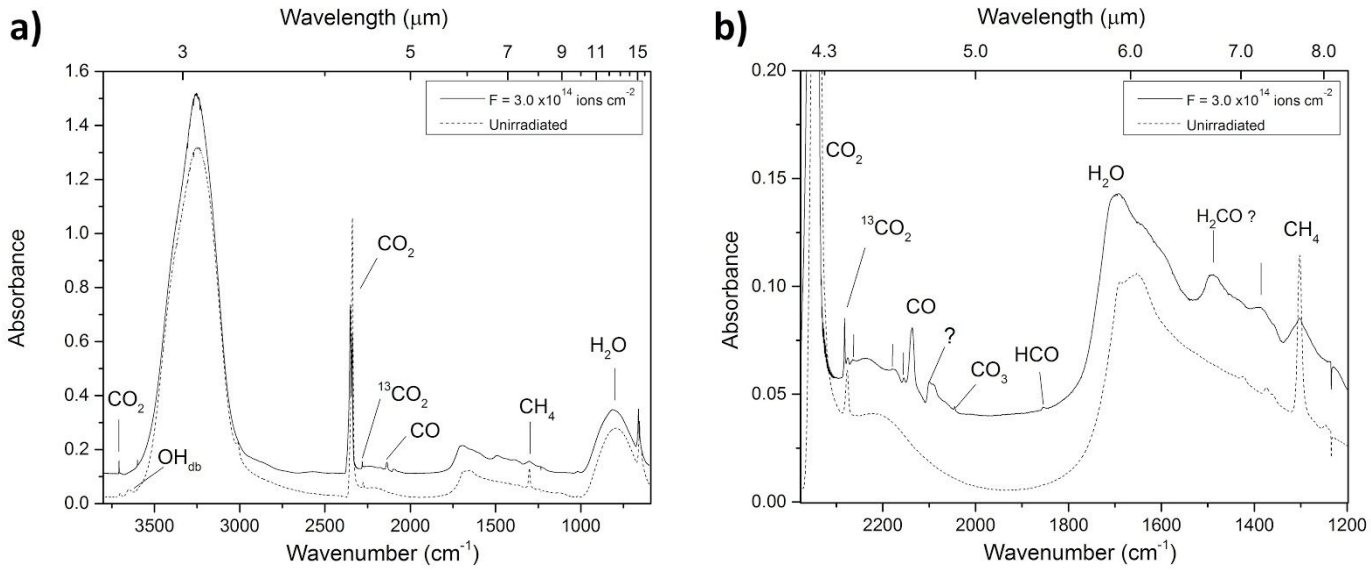

Figure 3: #SI-1 experiment. a) Infrared spectra of H_2O:CO_2:CH_4 (10:1:1) ice before irradiation (dashed line) and after irradiation with $^{16}O^{+5}$ 15.7 MeV at a fluence of 3.0×10^{14} ions cm^{-2} (full line); b) zoomed - in region around 2400 – 1200 cm^{-1}.

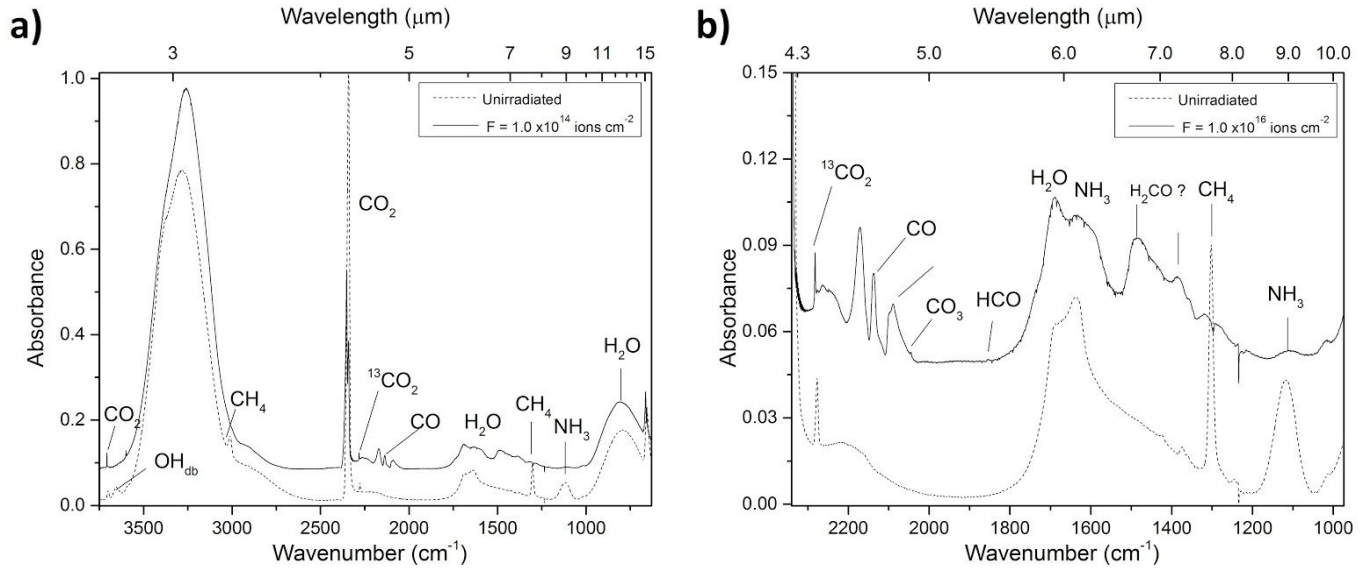

Figure 4: #SI-2 experiment. Infrared spectra of H_2O:CO_2:CH_4:NH_3 (10:1:1:1) ice before irradiation (dashed line) and after irradiation with $^{16}O^{+5}$ 15.7 MeV at a fluence of 1.0×10^{14} ions cm^{-2} (full line); b) zoomed - in region around 2400 – 1200 cm^{-1}.

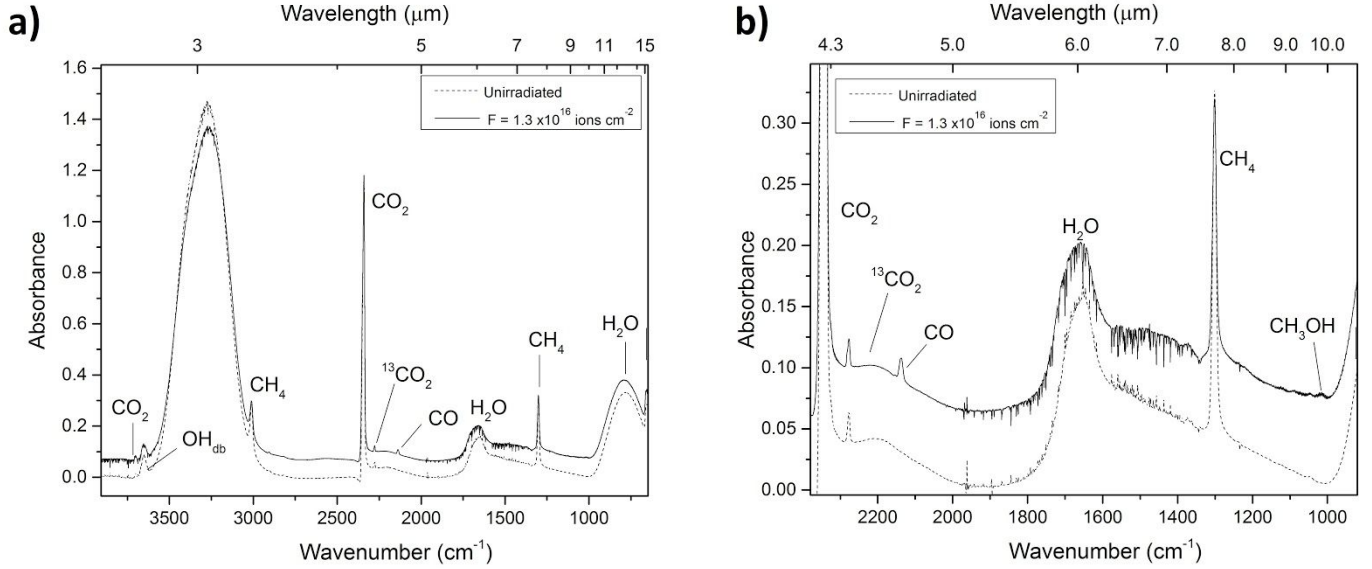

Figure 5: #LI-1 experiment. a) Infrared spectra of H_2O:CO_2:CH_4 (10:1:1) ice before irradiation (dashed line) and after irradiation with $^{16}O^{+6}$ 108 keV at a fluence of 1.3×10^{16} ions cm^{-2} (full line); b) zoomed - in region around 2400 – 1200 cm^{-1}.

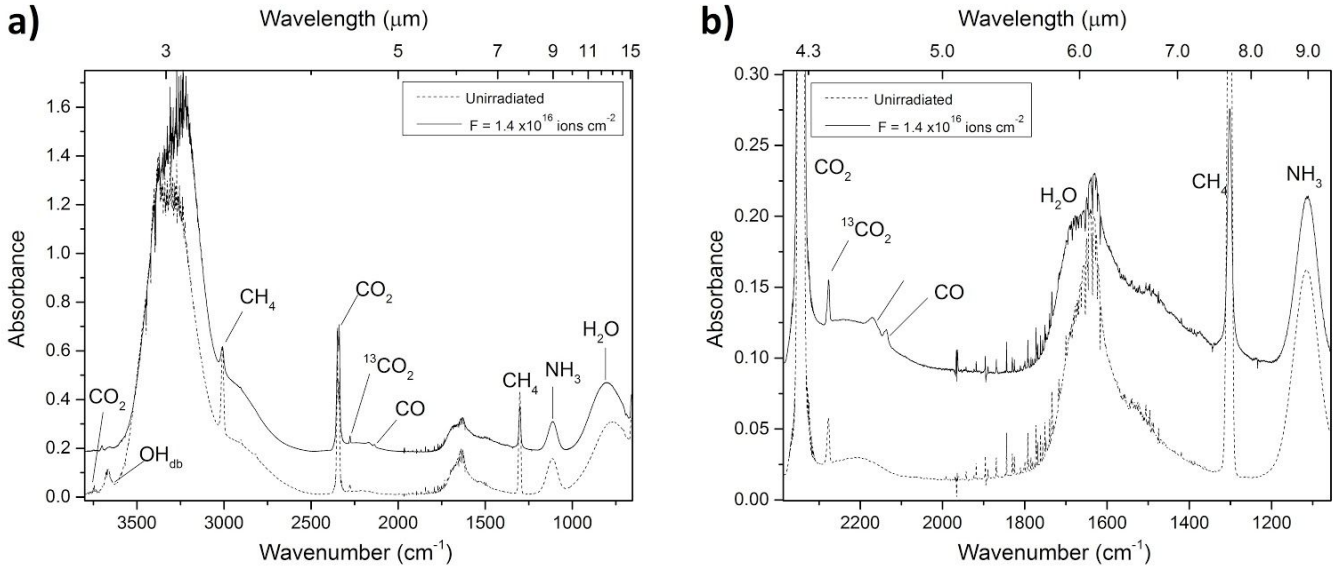

Figure 6: #LI-2 experiment. a) Infrared spectra of H_2O:CO_2:CH_4:NH_3 (10:1:1:1) ice before irradiation (dashed line) and after irradiation with $^{16}O^{+6}$ 108 keV at a fluence of 1.2 ×10^{16} ions cm^{-2} (full line); b) zoomed - in region around 2400 – 1200 cm^{-1}.

The infrared bands used to quantify the column density of the parent species (using Equation (1)) as well as the corresponding A-values are listed in Table 2. The bands used to identify and quantify the daughter species, as well as their assignment, are summarized in Table 3.

Table 2: Bands in the IR spectra used to quantify the parent species in the icy samples.

H_2O:CO_2:CH_4 (10:1:1) ices				
Band position in exp. #SI-1	**Band position in exp. #LI-1**	**Assignment (vib. Mode)**	**A-value (cm molecule^{-1})**	**Ref.**
794	784	H_2O (libration)	2.6×10^{-17}	d'Hendecourt & Allamandola 1986
2340	2341	CO_2 (v3)	7.3×10^{-17}	Gerakines et al. 1995
1302	1301	CH_4 (v4)	6.1×10^{-18}	d'Hendecourt & Allamandola 1986
H_2O:CO_2:CH_4:NH_3 (10:1:1:1) ices				
Band position in exp . #SI-2	**Band position in exp. #LI-2**	**Assignment (vib. Mode)**	**A-value (cm molecule^{-1})**	**Ref.**
795	781	H_2O (libration)	2.6×10^{-17}	d'Hendecourt & Allamandola 1986
2341	2280*	CO_2 (v3)	7.3×10^{-17}	Gerakines et al. 1995
1302	1302	CH_4 (v4)	6.1×10^{-18}	d'Hendecourt & Allamandola 1986
1119	1116	NH_3 (v3)	1.4×10^{-17}	Zanchet et al. 2013

*The v3 mode of CO_2 was saturated. The v3 mode of $^{13}CO_2$ was used to quantify CO_2 in the sample

Table 3: Bands of daughter species in the IR spectra of H_2O:CO_2:CH_4 (10:1:1) and H_2O:CO_2:CH_4:NH_3 (10:1:1:1) ices irradiated with $^{16}O^{+6}$ 108 keV and $^{16}O^{+5}$ 15.7 MeV ions.

H_2O:CO_2:CH_4 (10:1:1) ices				
Band position in exp. #SI-1	**Band position in exp. #LI-1**	**Assignment**	**A-value (cm molecule^{-1})**	**Ref.**
1017	1015	CH_3OH	1.4×10^{-17}	d'Hendecourt & Allamandola (1986)
1388*	-	-	-	-

1488**	-	H_2CO	-	Pilling et al. 2010b
1855	-	HCO	2.1×10^{-17}	d'Hendecourt & Allamandola (1986)
2045	-	CO_3	8.9×10^{-18}	Bennett et al. (2004)
2137	2138	CO	1.1×10^{-17}	d'Hendecourt & Allamandola (1986)
2154*	-	-	-	-
2176*	-	-	-	-
2265*	-	-	-	-
H_2O:CO_2:CH_4:NH_3 (10:1:1:1) ices				
Band position in exp. #SI-2	**Band position in exp. #LI-2**	**Assignment**	**A-value**	**Ref.**
1015	-	CH_3OH	1.4×10^{-17}	d'Hendecourt & Allamandola (1986)
1357*	-	-	-	-
-	1374*	-	-	-
1385*	-	-	-	-
1484**	-	H_2CO	-	Pilling et al. 2010b
1855	-	HCO	2.1×10^{-17}	d'Hendecourt & Allamandola (1986)
2045	-	CO_3	8.9×10^{-18}	Bennett et al. (2004)
2089	-	CN^-	1.8×10^{-17}	Moore et al. (1983), Augé (2016)
2097	-	HCN	5.1×10^{-18}	Burgdorf et al. (2010), Augé (2016)
2137	2137	CO	1.1×10^{-18}	d'Hendecourt & Allamandola (1986)
2171	2171	OCN^-	1.3×10^{-16}	Moore et al. (1983) van Broekhuizen et al. (2004)
2263**	-	HNCO	-	Lowenthal et al. (2002)

*Features that were not assigned;

**Tentative assignments

From Table 3, it is possible to note that MeV ions induce the synthesis of more species than the keV ions. The daughter species HCN, CN^- HCO, HNCO, and CO_3 are produced only in the samples irradiated by MeV ions. This may be related to the fact that these ions ionize even the inner shells of light target atoms, such as C,N, and O, which completely destroys the molecules and thus produces free radicals. This opens reaction pathways that do not appear for the lower energy projectiles.

3.1 Molecular cross-section

From the evolution of column density as a function of fluence, it is possible to calculate the effective dissociation and formation cross-sections of the parent and daughter species, respectively, following the equation (adapted from Pilling et al. 2010a, 2010b):

$$N(F) - N_0 = N_{inf}\left(1 - \exp\left(-\sigma_{d,f}F\right)\right) - YF \quad \text{[molecules cm}^{-2}\text{]} \qquad (3)$$

where F is the ion fluence, in units of cm^{-2}; $N(F)$ is the column density of the molecular species at fluence F; N_0 is the column density of such species in the non-irradiated sample; σ is the effective destruction cross section (σ_d) or the effective formation cross section (σ_f), all in cm^2; Y is the sputtering yield, in molecules per ion (see also Vasconcelos et al. 2017a, 2017b); and N_{inf} is a constant, in units of cm^{-2}. Most of the parent species were modeled considering Y = 0. This approach was preferred because some species are formed in the bulk of the ice, being less affected by a surface process like sputtering. The species for which Equation 3 was better adjusted by including the sputtering term are indicated in Table 4. For a more formal and detailed discussion about the variation of sputtering with the ice thickness, we refer the reader to Dartois et al. 2018.

The values for effective destruction and formation cross-sections for parent and daughter species, respectively, are shown in Table 4. Figure 7 shows the measured column density of the parent and daughter species as a function of the ion fluence along with the fit of Equation 3.

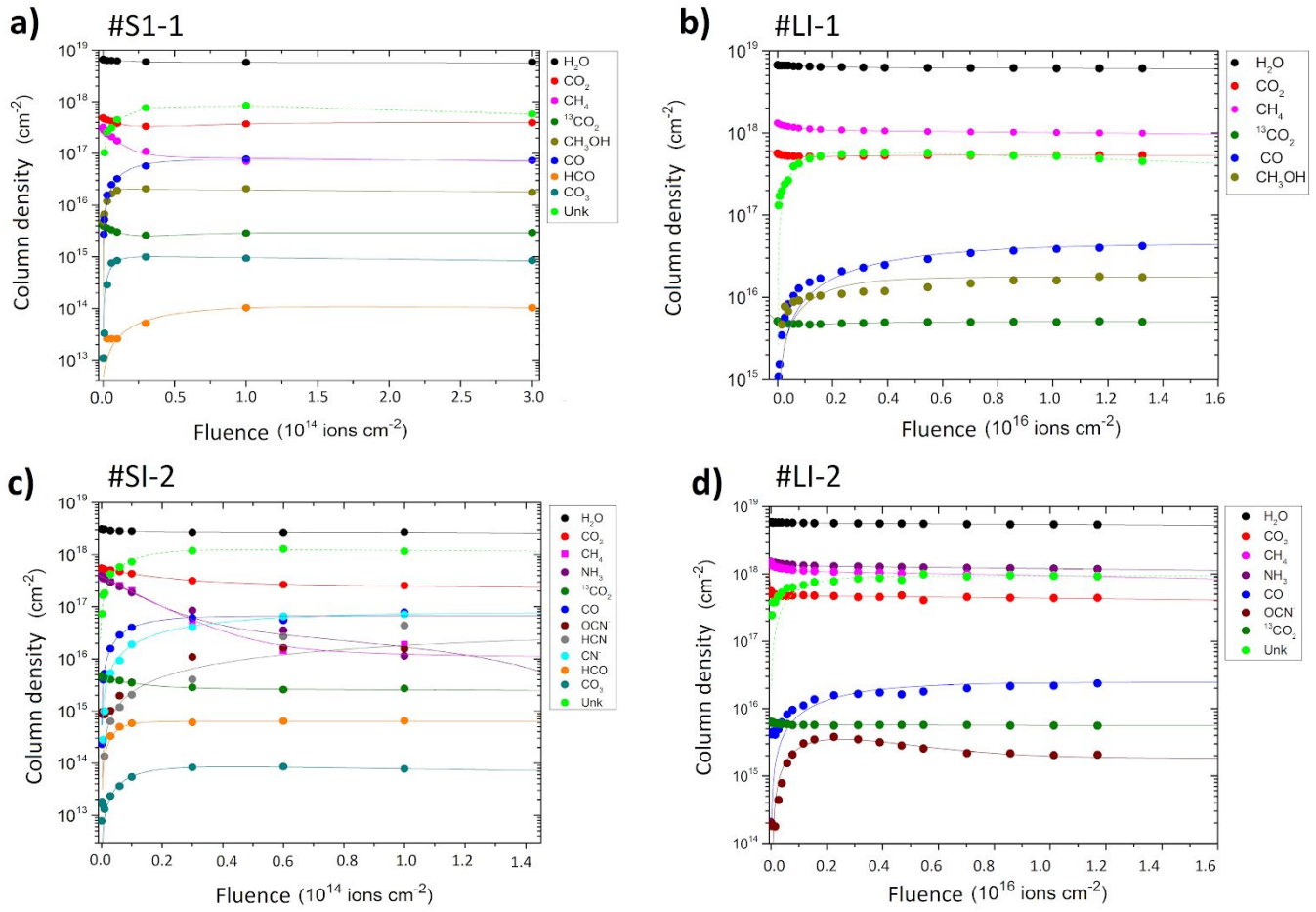

Figure 7 – Column density of selected species as a function of fluence for experiments a) #SI-1; b) #LI-1; c) #SI-2, d)#li-2. Lines are the best fits obtained with equation 3. As discussed in Appendices A and B, "Unk" indicates the column density of the species that are not identified by IR spectroscopy. See details in the text.

The cross-sections obtained for the MeV ions experiments are in the range 10^{-13} - 10^{-14} cm^2 , the same order of magnitude as those reported for previous experiments on ion irradiation of pure or mixed ices performed by our group with similar instrumentation (e.g. Vasconcelos et al. 2017a; 2017b; 2017c; Pilling et al. 2010a; 2010b). The cross-sections for the experiments with keV ions are of the order of 10^{-15} cm^2 and 10^{-16} cm^2. These values are about two orders of magnitude smaller than the effective cross-sections obtained for MeV ions, also in agreement with values from irradiation experiments with ions of similar energy (Gomis et al. 2005). A point worth stressing is that the term "effective" means that these values depend on the chemical environment of the icy samples.

Table 4: Effective destruction cross section (σ_d) of parent species and effective formation cross section (σ_f) of daughter species in the studied ices. The bands used to monitor the column density of each species are also shown. Estimated errors are around 20%.

Parent species		**σ_d (10^{-13}cm^2)**		**σ_d (10^{-15}cm^2)**	
Molecule	**v (cm^{-1})**	**#SI-1**	**#SI-2**	**#LI-1**	**# LI-2**
H_2O	800	0.7 ± 0.6	1.9 ± 0.4	0.7 ± 0.1	1.0 ± 0.4
CO_2	2342[a]	1.0 ± 0.1	0.50 ± 0.03	2.5 ± 0.3	*
CH_4	1301	0.9 ± 0.1	0.8 ± 0.1	1.6 ± 0.1	3.0 ± 0.2
NH_3	1117	-	1.1 ± 0.1	-	1.6 ± 0.1
Daughter species		**σ_f (10^{-13}cm^2)**		**σ_f (10^{-15}cm^2)**	

Molecule	v (cm^{-1})	#SI-1	#SI-2	#LI-1	#LI-2
CO	2138	5.5 ± 0.6	0.9 ± 0.2	0.260 ± 0.004	0.4 ± 0.05
OCN^-	2170	-	0.3 ± 0.03	-	1.0 ± 0.2 **
CH_3OH	1017	3.0 ± 1.0	1.9 ± 0.2	5.2 ± 0.9	-
CO_3	2045	0.2 ± 0.1	0.9 ± 0.2	-	-
HCO	1854	1.6 ± 0.3	2.1 ± 0.3	-	-
CN-	2092	-	0.27 ± 0.03	-	-
HCN	2100	-	0.09 ± 0.01	-	-

*Since the band assigned to v3 mode of CO_2 could be saturated, the band chosen to monitor the column density of CO_2 in the experiment with ammonia irradiated with 108 keV ions was the combination mode v1 + v3, around 3700 cm^{-1}.

**Daughter species adjusted with the sputtering term (Equation 3)

3.2 Destruction of the parent species

The percentage of each parent species destroyed after irradiation (D%) can be quantified by the equation:

$$D\% = 100 * \frac{No-Nf}{No} \quad [\%] \tag{4}$$

where *No* and *Nf* indicate the column density of a given parent species before irradiation and after irradiation (at maximum fluence), respectively. The calculated values are listed in Table 5.

Table 5: Percentage of the destroyed parent species molecules (D%) in the four experiments, with and without ammonia during radiolysis up to the final projectile fluence. Projectile energy and maximum fluence are also indicated.

Molecules	H_2O:CO_2:CH_4 (10:1:1)		H_2O:CO_2:CH_4:NH_3 (10:1:1:1)	
	#LI-1	#SI-1	#LI-2	#SI-2
H_2O	9.3 %	9.5 %	7.4 %	12.5 %
CO_2	5.5 %	20.1 %	20.9 %	53.9 %
CH_4	24.5 %	77.0%	37.1 %	95.4 %
NH_3	-	-	21.2 %	97.1 %
Maximum ion Fluence (ion cm^{-2})	1.3×10^{16}	3.0×10^{14}	1.2×10^{16}	1.0×10^{14}
Maximum Energy Fluence Delivered (eV cm^{-2})	1.4×10^{21}	4.7×10^{17a}	1.4×10^{21}	1.0×10^{17a}

[a] Considering the energy delivered of ~ 1570 eV and ~1070 as illustrated in Fig 2 for experiments **#SI-1** and **#SI-1**, respectively. The projectile range is larger than the sample thicknesses so that the incoming ions pass through the sample, depositing only a fraction of their kinetic energy.

As can be seen from Table 5, the MeV projectiles destroy more parent molecules than 108 keV projectiles, being methane and ammonia the more depleted species. Moreover, it seems that in the presence of NH_3, the depletion of CH_4 is higher. This could be due to the reaction of species produced from methane radiolysis with NH_3 (or also with species produced from ammonia radiolysis), but further investigation would be necessary to reach any conclusion.

3.3 Chemical Equilibrium and Equilibrium Branching Ratio (EBR%)

At low irradiation fluences we observe that the molecular column densities decrease for parent species and increase for daughter species. At high fluences, the molecular column density reaches a plateau (and at even higher fluences, the sputtering becomes predominant and N(F)

decays linearly in time). For irradiation experiments with ions, when the regime at which the column densities decrease linearly with fluence is reached, the net formation or destruction of molecular species no longer occurs, but only the depletion due to sputtering. So, we refer here to "chemical equilibrium" as the regime where the variation in column density of a species is only due to the sputtering process (see also Bonfim et al. 2017, Vasconcelos et al. 2017b, 2017c). At the fluence at which the sample reaches the chemical equilibrium, the "final" composition of a sample under irradiation can be determined. The criteria and procedure for determining the point at which the sample is in equilibrium is described in the Appendix B.

Table 7 shows the equilibrium fluence F_E, calculated using the methods described in Appendix B, the energy fluence at this point (E_E) and electronic local dose ,D_e (i.e. the energy projectile energy that is transferred to the electrons of the target material). The electronic local dose D_e, in units of eV molecule^{-1} is calculated with the equation:

$$D_e = 10^7 \phi \times t \times S_e \frac{M}{\rho N_A} \quad (eV molecule^{-1}), \tag{5}$$

where φ is the ion flux, in units of ions cm^{-2} s^{-1}; t is the irradiation time (or exposure time) in seconds; S_e is the integrated electronic stopping power considering penetration up to a depth where the projectile ion has stopped completely (see Figure 2), in units of keV; M is the initial average molecular mass of the sample in g per mol: ρ is the average sample density in g cm^{-3}; N_A is Avogadro's Number; and S_e is the energy transferred to the sample during electronic interaction between the projectile and the atomic targets. The average density of the samples was estimated by considering the weighted average of each parent species, assuming their densities for pure ice.

The values of energy deposited per molecule, or electronic local dose, to reach the chemical equilibrium (D_e) are higher for the experiments with 108 keV ions (144 and 63 eV molecule^{-1}) than the values for the experiments with swift ions (170 and 144 eV molecule^{-1}). This result shows that, for samples irradiated with MeV ions, less energy is needed to reach the equilibrium when compared to 108 keV ion bombardment. To explain this difference, one must consider the way in which each projectile loses energy when interacting with target atoms. The slower 108 keV oxygen ions lose more than half of their energy in nuclear interactions with the atoms of the bombarded material (see Figure 2 panel b), while 15.7 MeV oxygen ions interact almost mainly electronically with the target atoms (Figure 2 panel a). The nuclear interaction of the ions with target nuclei can result in collisions that displace atoms of the target molecules within the sample, resulting in the dissociation of the formed molecules. However, the reason why the samples irradiated with MeV ions require a smaller input of energy is still not understood.

From the values in Table 6, it is possible to notice that samples containing NH_3 show lower values of equilibrium fluence than the experiments without NH_3. This could indicate that the daughter species that originate from ammonia may be more stable.

Table 6: Equilibrium fluence (F_E), energy fluence at chemical equilibrium (E_E) and electronic local dose (De_E) at chemical equilibrium for all experiments

Experiment	Eq. fluence (F_E) (ions·cm^{-2})	Energy fluence at equilibrium E_E (eV·cm^{-2})	Electronic local dose at Equilibrium De_E (eV·molecule^{-1})
#SI-1	1.8×10^{14}	2.8×10^{21}	144
#SI-2[a]	1.3×10^{14}	2.0×10^{21}	63
#LI-1	8.1×10^{15}	8.7×10^{20}	170
#LI-2[a]	7.0×10^{15}	7.6×10^{20}	140

[a] Samples with ammonia.

Knowing the equilibrium fluence, the percentage abundances of the molecular species in equilibrium, the "Equilibrium Branching Ratio" (EBR%), can be calculated by:

$$EBR_i\% = \left(100 \times \frac{Ni}{\sum_{i=all} Ni} \right)_{At\ equilibrium} \quad [\%], \tag{6}$$

where N_i indicates the column density of a species at the equilibrium fluence. In this equation, the sum takes into account all parent and daughter species at this fluence, including species present in the ice that can not be detected using the IR spectroscopy (called here "unknown species"). Such unknown species include molecules with abundances below the detection limit of the spectrometer, molecules with IR bands being highly convoluted with other bands and molecules that are not detectable in the infrared but may be present in the ice. The procedure for estimating the column density of these species is described in Appendix A. The EBR for the produced species are

Table 7: Equilibrium Branching Ratio (EBR%), in percentage, for the parent species and identified new produced species in all the experiments. The values were calculated using Equation (6). Estimated values for unidentified species were also given (see details in the text).

	Experiment with MeV ions		**Experiments with 108 keV ions**	
Molecule	#SI-1	#SI-2[a]	#LI-1	#LI-2[a]
H_2O	77.4	62.8	74.1	59.4
CO_2	5.3	6.5	6.5	4.8
CH4	1.0	0.3	12.4	10.8
$^{13}CO_2$	0.04	0.1	0.06	0.06
NH_3	-	0.2	-	13.4
CN^-	-	1.8	-	-
HCN	-	1.0	-	-
CO	1.0	1.6	0.5	0.2
CH_3OH	0.2	0.1	0.2	-
OCN^-	-	0.4	-	0.03
HCO	0.01	0.02	-	-
CO_3	0.002	0.002	-	-
Unknown	15.1	26.1	6.3	11.2

[a] Sample with ammonia initially.

The EBR% of daughter species are larger in samples bombarded with MeV ions when compared with the same species in the samples bombarded with keV ions. In the case of CO, the EBR % are 1.0% and 1.6%, in experiments #SI-1 and #SI-2, respectively, in contrast with 0.5% and 0.2% in experiments #LI-1 and #LI-2, respectively. For the OCN^-, the EBR% value is roughly 10 times higher for MeV ion irradiation when compared to the keV irradiated ices, being the values 0.4% and 0.03% for the #SI-2 and #LI-2, respectively.

In the case of Methanol (CH_3OH), as can be seen in table 7, the presence of NH_3 in the ice can influence the reaction pathways for this species during radiolysis. Indeed, the corresponding EBR% value is only half of that observed without the presence of NH_3 for MeV ion irradiation. The effect is even more pronounced in the case of 108 keV ions: in this case, EBR%=0. Interestingly, however, the presence of ammonia seems to enhance the production of unknown species during ion bombardment. This might suggest that a large fraction of the unknown species may contain nitrogen atoms. A future investigation will help to clarify this issue.

The EBR% of CO_3 are virtually the same in the two projectile energy regimes. This indicates that ammonia does not play a significant role in the reaction pathways for this species, although it seems to have some influence in the production of CO and CH_3OH, and HCO.

4. Implications on Enceladus chemistry scenario

The analyzed samples are case studies and could represent aspects of physicochemical processes induced by the bombardment of icy surfaces in space with energetic ions (cosmic rays, magnetospheric particles, solar wind or solar energetic particles). Examples are frozen moons around giant planets, KBOs (Kuiper Belt Objects) and TNOs (Transneptunian Objects), comets, protoplanetary ices and other frozen surfaces in evolved planetary systems, as well as dust grains in molecular clouds. In this section, we focus on the astrophysical implications of this work for one particular example, the Saturnian moon Enceladus.

The ice particles and gas in Enceladus plumes were already proven to contain many organic species (see Postberg et al. 2018b for a review about the Enceladus plume and surface composition). These particles, arising from Enceladus interior, are constantly falling onto the moon's surface and feeding the Saturnian E-ring, making the composition of the frozen material more complex. In addition, the solid material is continuously affected by ionizing radiation that forms and destroys species and changes the physical properties of the frozen material. It follows that the species produced by the charged particles analyzed here are just a fraction of the chemical processes that take place on the solid bodies in Enceladus. Most of the species can be sequentially destroyed by other types of radiation (e.g. incoming UV and X-rays photons, electrons and other charged particles in Saturn's magnetosphere), so the abundances obtained by this work can just be linked to the Enceladus environment in combination with other laboratory experiments and the data taken in the different Cassini's flybys.

In all the irradiated ices, CO is amongst the most produced species (not considering species that are included in the "unknown species"). The CO abundance (EBR(%)) is between 1.0 - 1.6 % in all the irradiated ices (see Table 7). These values are higher than the upper limit of 0.2% estimated for CO in the Enceladus plumes (Postberg et al. 2018b). The higher abundances of CO in the irradiated ices when compared with Cassini data can be due to the fact that CO_2, the parent species of CO, present in a final abundance of 4.8 - 6.5 % in our experiments, is present in the Enceladus plumes in smaller ratios, between 0.3 - 0.8% (Postberg et al. 2018b) . The subsequent photoprocessing and radiolysis of CO, induced by other energetic agents, may also be responsible for the lower abundances of this species in Enceladus plumes.

The planetesimals that formed Enceladus may have brought some species detected in plumes during the CASSINI flybys. This may be the case for HCN, that is present in Enceladus plume at maximum abundance of 0.2%. In the presence of warm water, HCN is quickly hydrolyzed to HCOOH and NH_3 (Miyakawa et al. 2002), indicating that this species does not arise from Enceladus' interior. This molecule may have been brought to Enceladus within primordial material (Waite et al. 2009) or it may have formed *in-situ* at Enceladus' surface. In the NH3 containing samples irradiated with MeV ions, HCN is formed, and it is present in a quantity of 1% in the chemical equilibrium. Curiously, the irradiation of water-rich ices of similar composition by 1 keV

electrons (Bergantini et al. 2014a), 5 keV electrons and VUV/soft X-rays photons (Pilling et al. 2019), this species was not detected. This indicates that, if HCN is formed *in-situ* in Enceladus, charged particles may play a crucial role in the synthesis of this species.

In the same way as HCN, HCNO was also produced in the NH_3-containing ice irradiated by MeV ions but not in similar experiments involving the irradiation by electrons and VUV and X-rays photons. This species has mass 43 a.u., but it has not been assigned in the mass spectra taken by INMS. However, the assignment of carbon-bearing species in this region presents some ambiguities, and better assignments would require higher-resolution mass spectra (Postberg et al. 2018b).

In all irradiations of NH_3 containing samples discussed here, the cyanate ions (OCN^-) were detected after radiolysis. This species was also detected in the irradiation of ices with similar composition and temperature by 1 keV electrons (Bergantini et al. 2014a), VUV and X-rays photons (Pilling et al. 2019). The OCN- is a common species present in the energetic processing of ammonia-containing samples in the presence of molecules such as CO_2, CH_4 and H_2O (Broekhuizen et al. 2004) We note that the efficiency of OCN^- production by 1 keV electrons (roughly estimated by $N_{OCN^-}/(N_{H2O} + N_{CO2} + N_{NH3})$ taken from Bergantini et al. 2014a), seems to be less than the observed in the ion irradiation experiments. The EBR of OCN- for the MeV ion experiments is however comparable to the EBR of the same species in VUV-soft X-rays irradiation of ices : 0.4 % for the MeV ion irradiation and 0.5% for the VUV- soft X-rays irradiation (Pilling et al., 2019). Besides being easily formed by the energetic processing of ices with composition similar to Enceladus moon, the cyanate ions were not detected by the Cassini measurements. Negatively charged molecules can be detected by the Cassini's Electron Spectrometer (ELS), part of the CAPS instrument. The species detected in the mass spectra taken in the Enceladus plumes are mainly associated with negatively charged water clusters (Coates et al. 2010) and high mass species, with no conclusive assignment so far. Coates cited that these negatively charged clusters have a short lifetime in the enceladus plume environments where collisions with neutrals, positive charged particles, and grains, are frequent. This can also be the case for other anionic species, so the presence of these negatively charged species in the plume environment is not expected. *In-situ* investigations of the Enceladus icy surface would reveal the presence of anionic species (such as OCN-) in regions where the ice is processed by energetic particles and photons, since negatively charged particles could have a longer life-time when embedded in the ice.

Another anionic species identified in our experiments, the CN-, was synthetized in detectable quantities only in the MeV irradiation experiment, what is expected, since the formation route of this molecule is probably linked to the formation of HCN (also detected only in the MeV ion experiment). However, this species was not detected in Enceladus. The reasons may involve difficulties in the detection of anionic species in the Enceladus environment, as cited before.

With the knowledge of the ion flux in a given cold space environment and with the determined EBR% and the sputtering yield *Y,* we can estimate the individual flux of molecular desorption from the surface ($\psi_{Ei,space}$), in units of molecules cm^{-2} s^{-1} from:

$$\psi_{Ei,space} = \frac{EBR\%_i}{100} \times Y \times \phi_{space} \quad \text{[molecules cm}^{-2}\text{ s}^{-1}\text{]} \qquad (8)$$

where the ion flux in space environment (ϕ_{space}) is in units of ions cm^{-2} s^{-1}. The sub-index $_E$ at $\psi_{Ei,space}$ is to remind us that this quantity was determined under the scenario of chemical equilibrium in the sample. By summing the contribution of all desorbed species (including estimated unknown ones) after reaching chemical equilibrium we obtain the total desorption flux $\left(\psi_{Ei,space}\right)$ in space environment as

$$\psi_{E,space} = \sum_{i=all} \psi_{Ei,space} = \frac{EBR\%_i}{100} \times Y \times \phi_{space} \quad \text{[molecules cm}^{-2}\text{ s}^{-1}\text{]} \; . \qquad (9)$$

Especially for Enceladus, the effects of incident O-containing ions are of great importance since these species are the main component of Saturn's magnetosphere plasma at its orbit (Sittler et al. 2005, Young et al. 2005). However, such a procedure might be applied to other cold Solar System surfaces in an attempt to elucidate the mechanisms that influence the formation of tiny atmospheres around these frozen surfaces. A future publication will handle this issue mode deeply, but a glimpse of preliminary calculations is given below.

Considering the sputtering yield of $Y = 10^3$ molecules ion^{-1} (for MeV ions), the flux of oxygen ions (with energy ~10 MeV) of the order of 10^4 ions cm^{-2} s^{-1} (roughly estimated from Jurac (2001)) and the EBR% of water (~70%), we have estimated that the rate at which H_2O molecules are sputtered from the icy surface is approximately 7 x 10^6 molecules cm^{-2}s^{-1} . This value is smaller than the rate of H_2O in Enceladus, estimated by Johnson et al. (2008) as nearly 10^8 - 10^9 molecules cm^{-2}s^{-1}. The value estimated by Johnson et al. takes into account the sputtering of water due to the magnetospheric ions of the water group (i.e. the sputtering due to the incidence of protons and other magnetospheric ions are not accounted for). Additionally, if we consider an icy body with the dimension of Enceladus (surface area ~8 x 10^{15} cm^2), the average rate of H_2O ejection by oxygen would be roughly 6 x 10^{22} H_2O s^{-1}. For a matter of comparison, this value is orders of magnitude lower than the amount of H_2O ejected by the plumes at the south pole of Enceladus (~ 10^{28} H_2O s^{-1}), and it is also lower than a secondary global contribution of H_2O molecules ejected by Enceladus (~ 10^{25} H_2O s^{-1}) detected by Cassini CIMS observations (Burger et al. 2007).

These comparisons would suggest that the water desorption induced processes at Enceladus' surface by the incoming MeV oxygen ions play a minor role in the production of gaseous species in the vicinity of this moon. Although the calculated desorption flux is smaller than observed, it is necessary to keep in mind that this estimative just takes into account the sputtering by oxygen ions with a specific energy. A more realistic comparison should be made considering a broader range of energies. Additionally, Enceladus' surface is constantly being refreshed by fluffy deposits from its plumes, which complicates even more the parameterization of gas-phase delivery induced by ion bombardment of the surface.

5. Conclusions

This work presents experimental results of the irradiation of H_2O:CO_2:CH_4 (10:1:1) and H_2O:CO_2:CH_4:NH_3 (10:1:1:1) ices at 72 K by 108 keV $^{16}O^{+5}$ ions and 15.7 MeV $^{16}O^{+6}$ ions. These experiments help to understand the chemical composition and chemical processes of ice surfaces of the outer Solar System (with focus on Enceladus) when exposed to bombardment by energetic particles. The physicochemical changes in the ices were monitored during the irradiation by infrared spectroscopy. The conclusions of the work are summarized below:

- The samples irradiated with MeV ions produced a more (detectable) diversity of daughter species, some of them not observed in the experiments using 108 keV ions. The species identified in the experiments with MeV ions are: CO, OCN, CO_3 , HCO, H_2CO, H_2CO_3, CH_3OH, HNCO, CN^- , HCN and CN^- ; and the ones identified in the experiment with keV ions are: CO, OCN and CH_3OH. In all the experiments, the CO is amongst the most abundant produced species (considering just the ones identified and quantified by IR spectroscopy).
- The effective destruction cross-sections of the parent species and the effective formation cross-sections of the daughter species were calculated. The effective formation cross-section for the new species is within the 10^{-15} - 10^{-16} cm^2 range for the experiments using 108 keV ions as projectiles and 10^{-13} - 10^{-14} cm^2 for the experiments using 15.7 MeV ions.

- The ices irradiated with MeV ions presented higher depletions of NH_3 and CH_4 (destruction larger than 95%) when compared to the ice bombarded with keV ions.
- The molecular abundances at chemical equilibrium (quantified by equilibrium branching ratios – EBR%) were quantified. These quantities are important because they give the abundances of the molecules present in the ice samples after long irradiation times (please, see details in the text).
- An estimative of the abundance of the species that are not quantified by the infrared spectroscopy is presented (these species are referred to in this work as "unknown species"). The abundance of the unknown species (estimated in solid samples after the bombardment) was larger in the samples irradiated by MeV ions experiments, suggesting that these samples may be even more chemically complex.
- The desorption of water molecules induced by the ion sputtering process was estimated and extrapolated to the Enceladus environment. The experimental data suggest that the ion desorption of water molecules by 15.7 MeV oxygen ions from the entire surface area of Enceladus would be around 7 x 10^{22} H_2O s^{-1} for MeV ions, a value that is order of magnitude smaller than the water ejected by Enceladus plumes.

The results found in this work help us to understand the effect of charged particles in cold astrophysical environments. The discussion about chemical equilibrium in solid phase in the presence of ionizing radiation after large fluences suggests that charged particles may largely modulate the chemistry in astrophysical environments, inducing similar composition in different lines of sights and locations in the galaxy, as well as in other cold space environments.

Acknowledgements

The authors acknowledge the Brazilian agencies FAPESP (Projects #2016/11334-5, #2017/07283-9, #2016/22018-7 and #2013/07657-5) and CNPq (Projects # 304130/2012-5 and #306145/2015-4) for financial support. We also thank the staff of CIMAP and GANIL for technical support. The experiments were performed at GANIL.

References

Augé B., Dartois E., Engrand C., Duprat J., Godard M., Delauche L., Bardin,N., Mejía C., Martinez R., Muniz G., Domaracka A., Boduch P., Rothard H., 2016, A&A, 592

Bennett C. J., Jamieson C. S., Mebel A. M., Kaiser R. I., 2004, Physical Chemistry Chemical Physics, 6, 735

Bergantini A., Pilling S., Nair B. G., Mason N. J., Fraser H. J., 2014a, A&A, 570, A120

Bergantini A., Pilling S., Rothard H., Boduch B., Andrade D. P. P., 2014b, MNRAS, 437, 2720

Bergantini A., 2015, PhD thesis, UNIVAP-Brazil (Portuguese only) https://www1.univap.br/gaa/teses/

Bonfim V. S., Castilho R. B., Baptista L., Pilling S., 2017, Physical Chemistry Chemical Physics, 19, 26906

van Broekhuizen F. A., Keane J. V., Schutte, W. A., 2004, A&A, 415, 425

Brown R. H., Clark R. N., Buratti B.J.M, Cruikshank D.P., Barnes J.W., Mastrapa R.M.E., Bauer J. et al., 2006, Science, 311, 1425

Brunetto R., Caniglia G., Baratta G.A., Palumbo M.E., 2008, ApJ, 686,1480

Burgdorf M., Cruikshank D.P., Dalle Ore C.M., Sekiguchi T., Nakamura R., Orton G., Quirico E., Schmitt B., 2010, ApJL, 718, L53

Burger M. H., Sittler Jr. E.C., Johnson R. E., Smith H.T., Tucker O.J., Shematovich V.I., 2007, J. Geoph. Research, 112, A06219

Coates A.J., Jones G.H., Lewis G.R., Wellbrock A., Young D.T., Crary F.J., Johnson R.E., Cassidy T.A., Hill T.W., 2010, Icarus, Volume 206, Issue 2, Pages 618-622.

Combe F., McCord T. B., Matson D. L., Johnson T. V., Davies A.G., Scipioni F., Tosi F.,, 2019, Icarus, Volume 317, Pages 491-508

Dartois E., Chabot M., Id Barkach T., Rothard, H, Augé B., Agnihotri A. N., Domaracka A., Boduch P., 2018, A&A, 2018, Vol.618, p.A173

Duarte E., Domaracka A., Boduch P., Rothard H., Been T., Dartois E., Farenzena L. S., Silveira E. F., 2009, A&A, 502 2, 599-603

d'Hendecourt L. B., Allamandola L. J., 1986, A&AS, 64, 453

Gerakines P. A., Scutte W. A., Greenberg J. M., van Dishoeck E. F., 1995, A&A, 296, 810

Gomis O., Strazzulla G., 2005, Icarus, 177, 570

Hendrix A., Hansen C.J, Holsclaw G.M., 2010, Icarus, 206, 608

Johnson R. E., Famá M., Liu M., Baragiola R.A., Sittler E.C., Smith H.T., 2008, Planetary and Space Science, 56, 1238

Jurac S., Johnson R. E., Richardson J. D., Paranicas C., 2001, Planetary and Space Science, 49, 319

Kazeminejad B., Lebreton J.-P., Matson D. L., Spilker L.; Raulin F., 2002, The Cassini/Huygens mission to Saturn and Titan and its relevance to exo/astrobiology, Proceedings of the First European Workshop on Exo-Astrobiology, 16 - 19 September 2002, Graz, Austria. Ed.: Huguette Lacoste. ESA SP-518, Noordwijk, Netherlands: ESA Publications Division, ISBN 92-9092-828-X, pp. 261 – 266.

Lowenthal M., Khanna R., Moore M. H., 2002, Spectrochimica ActaPart A: Molecular and Biomolecular Spectroscopy, 58, 73

Lv X. Y., de Barros A. L. F., Boduch P., 2012, A&A, 546, A81

Matson D. L., Castillo J. C. Lunine J., Johnson T. V., 2007, Icarus, 187, 569

Miyakawa S., et al., 2002, Orig. Life Evol. Biosph. 32, 195

McKay C., Anbar A. D., Porco C., Tsou P., 2014, Astrobiology, 14, 352

Moore M. H., Donn B., Khanna R., A'Hearn M. F., 1983, Icarus, 54, 388

Parkinson C. D., Liang M.C., Yung Y. L., Kirschivnk J. L., 2008, Origins of Life and Evolution of the Biosphere, 38, 355

Pilling S., Duarte E.S., Silveira E.F., Balanzat E., Rothard H., Domaracka A., Boduch P., 2010a, A&A, 509, A87

Pilling S., Duarte E.S., Domaracka A., Rothard H., Boduch P., Silveira E.F., 2010b, A&A, 523, A77

Pilling S., Duarte E.S., Domaracka A., Rothard H., Boduch P., Silveira E.F., 2011, Physical Chemistry Chemical Physics, 13, 15755

Pilling S., Rocha W., Freitas F.M.,Silva P.A., 2019, RSC Adv, 9, 28823

Porco C., DiNino D., Nimmo F., 2014, AJ, 148, 45

Postberg F., Kempf S., Schimidt J., et al., 2009, Nature, 459, 1098

Postberg F. Khawaja N., Abel B., et al., 2018a, Nature, 558, 564

Postberg F. et al., 2018b, Plume and surface composition of Enceladus. In Enceladus and the Icy Moons of Saturn (P. M. Schenk et al., eds) pp 129-162. Univ. of Arizona, Tucson.

Raulin F., 2008, Astrobiology and Habitability of Titan. In: Botta O., Bada J.L., Gomez-Elvira J., Javaux E., Selsis F., Summons R. (eds) Strategies of Life Detection. Space Sciences Series of ISSI, vol 25. Springer, Boston, MA.

Rothard H., Domaracka A., Boduch P., Palumbo M. E., Strazzulla G., Silveira E. F. and Dartois E., 2017, J. Phys. B: At. Mol. Opt. Phys, v 50, 062001 (23pp)

Satorre M., et al., 2008, Planetary and Space Science, 56, 1748

Sittler Jr. E.C., et al., 2005, Geophys. Res. Lett., 32, L14S07

Spencer J.R., Pearl J. C., Segura M., et al., 2006, Science, 311, 1401

Southworth B.S, Kempf S., Spitale J., 2019, Icarus, V 319, Pg 33-42

Teolis, B.D., Perry M.E., Magee B. A., Westlake J., Waite J. H., 2010, J. Geophys. Res., 115, A09222,

Thomas P., Tajeddine R., Tiscareno M.S., Burns J.A., Joseph J., Loredo T.J., Helfenstein P., Porco C., 2016, Icarus 264, 37.

Vasconcelos F. A., Pilling S., Rocha W., Rothard H., Boduch P., Ding, J.J., 2017a, Physical Chemistry Chemical Physics, 19, 12845

Vasconcelos F. A., Pilling S., Rocha W., Rothard H., Boduch P., 2017b, Physical Chemistry Chemical Physics, 19, 24154

Vasconcelos F. A., Pilling S., Rocha W., Rothard H., Boduch P., Ding J.J., 2017c, ApJ, 850, 174

Young D.T., Berthelier J-J, Blanc M., Burch J.L., Bolton S., Coates A.J., Crary F.J., Goldstein R., Grande M., Hill T.W., et al., 2005. Science 307, 1262

Zanchet A., Rodriguez-Lazcano Y., Galvez O., Herrero V. J., Escribano R., Belén M., 2013, ApJ, 777, 26

Ziegler J. F.; Ziegler M. D.; Biersack J. P., 2010, Srim–the stopping and range of ions in matter (2010). Nuclear Instruments and Methods in Physics Research Section B:Beam Interactions with Materials and Atoms, 268, 1818. Available at http://www.srim.org/SRIM/SRIMLEGL.htm

Waite Jr. J. H., Lewis W. S., Magee B. A., et al., 2009, Nature, 460, 487

Appendix A: Column density of the "unknown species"

In this section, the procedure for estimating the mass and column density of the species that are not quantified by the IR technique is described. More details about this methodology are described in Vasconcelos et al. (2017c).

The column mass of a molecular species in the ice sample is given by:

$$M\ (F) = N\ (F) \times \overline{MM} \qquad \text{[Da cm}^{-2}\text{]}, \qquad \text{(A.1)}$$

where N (F) is the column density of the species, in units of molecule cm^{-2}, at fluence *F*, and $\overline{MM}$ is its molecular mass, in units of Da molecule^{-1}. The column density of a species that is sputtered from the ice surface, as a function of fluence, can be estimated as N (F) = Y x F, in which Y is the sputtering yield in units of molecules per incoming ion . Substituting this expression in Equation (A.1), the column mass of a desorbed species (i) is given by:

$$M_{des,i}(F) = Y \times F \times \overline{MM_i} \qquad \text{[Da cm}^{-2}\text{]}, \qquad \text{(A.2)}$$

The column mass of the species that are desorbed from the ice can be quantified using Equation (A.2) and the column mass of the species that are quantified by IR can be calculated using Equation (A.1). However, due to intrinsic limitations of IR spectroscopy, part of the molecules that remain in the ice cannot be identified and/or quantified. An estimate of the column mass of these species (that we call here "unknown species") can be done based on the conservation of mass: during the sample irradiation, the mass of the molecules on the solid sample plus the mass of the sputtered molecules should be constant, and equal to the initial mass of the sample. Taking this mass conservation and Equations A.1 and A.2 into account, the colum mass of the unknown species as a fluence of fluence is given by:

$$M_{UN}(F) = \sum_{i=parent} M_i(F=0) - \sum M_j(F) + M_{des,i}(F) \quad \text{[Da cm}^{-2}\text{]} \qquad \text{(A.3)}$$

where $\sum_{i=parent} M_i(F=0)$ is the column mass of the parent species in the initial sample (i.e., non-irradiated, F = 0), $\sum M_j(F)$ is the sum of the column masses of all the species in the ice sample at a given fluence *F* (this species are the ones quantified through the IR spectrum) and $M_{DES(F)}$ is the column mass of desorbed species at a fluence *F*, calculated using Equation (A.2).

Fig. A.1 shows the evolution of calculated column mass of the unknown species as a function of fluence. Displayed in the panels are: the column mass of the species in the ice that are quantified by IR spectroscopy ($M_{observed}$), the unknown species (M_{un}), calculated using Equation A.3, the desorbed species (M_{des}), calculated using Equation A.2, and the sum of all these column mass (M_{sum}). The values for the sputtering yield *Y* were initially estimate from Famá et al. (2008) and Rothard et al. (2017) and then "fine-tuned" to make the slope of the M_{un} curve at high fluences similar to the slope of the $M_{observed}$ curve at high fluences. This "fine-tuned" is made based on the assumption that the desorption rate of the unknown species is equal to the desorption rate of the observed species (in mass). After this procedure, the estimated values for sputtering yields Y in our experiments with MeV ions are 1000 and 1200 molecules ion^{-1} for the experiments #SI-1 and #SI-2, respectively. At lower projectile energy, Y was found to be 30 and 40 molecules ion^{-1}, for the experiments #LI-1 and #LI-2, respectively.

Considering the column mass of the non-observed species at a given fluence, M_{un} (F), and adopting a molar mass for these species, which we approximated to be equal to the average

molar mass of the parent species in the initial sample ($\overline{MM}_o$), the column density of the unknown species produced during the ion bombardment (N_{un}) can be estimated by:

$$N_{un}(F) = \frac{M_{un}(F)}{MMo} \qquad \text{[molecules cm}^{-2}\text{]} \qquad \text{(A.4)}$$

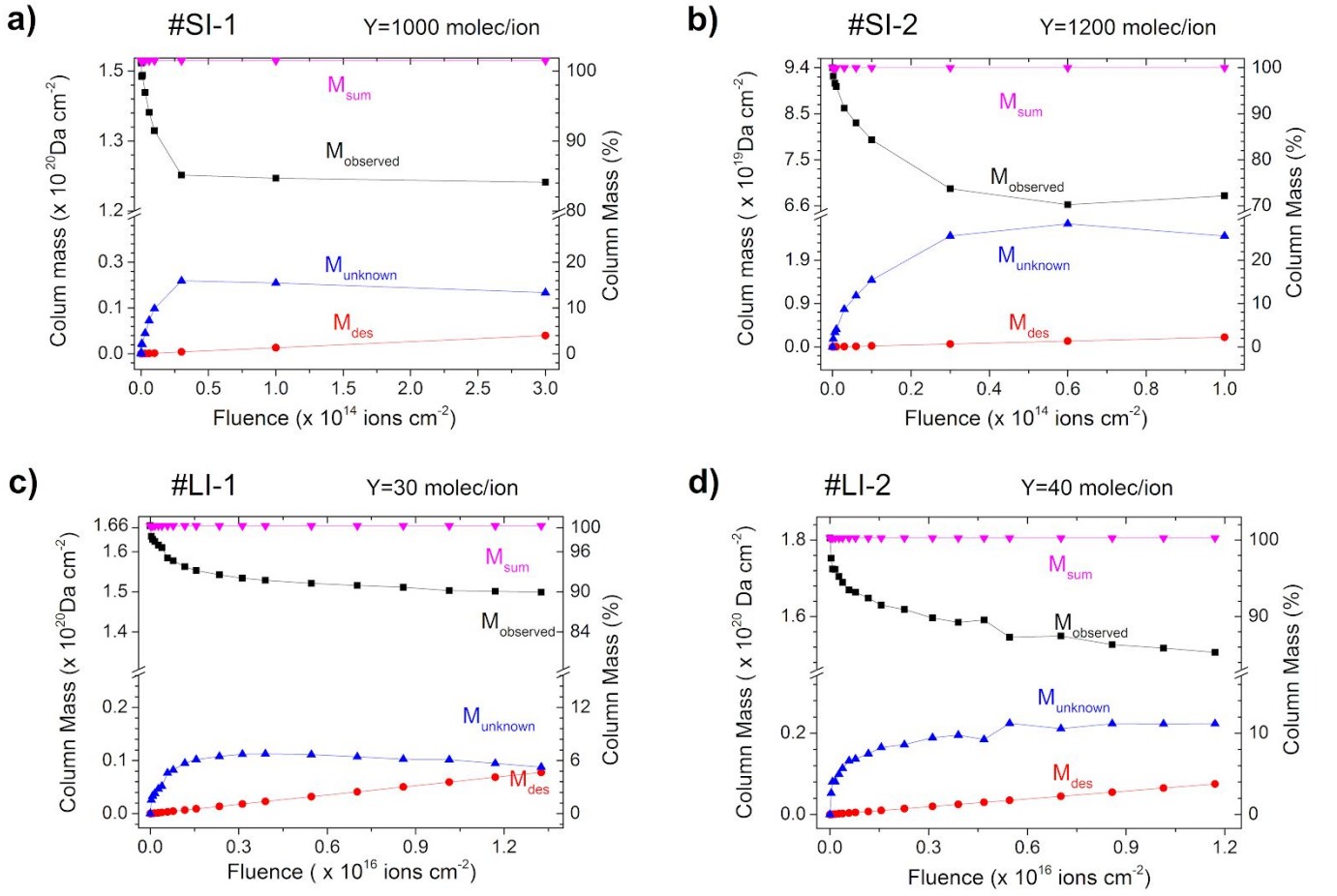

Figure A.1: Calculated column mass of the molecular species as a function of fluence for the experiments : a) #SI-1; b) #SI-2; c) #LI-1; d) #LI-2. Displayed in the panels are: i) the column density of the species that remain in the ice sample added to the mass of the species desorbed by sputtering, called M_{sum} (constant), in pink; ii) the sum of the column mass of the species quantified by IR spectroscopy, $M_{observed}$, in black; iii) the column mass of the species that are not quantified by IR spectroscopy but remain in the solid phase ,$M_{unknown}$ (calculated using Equation A.3), in blue; and iv) the column mass of the species that are sputtered from the ice, M_{des} (calculated using Equation A.2), in red. When $M_{observed}$ and $M_{unknown}$ reach a linear decrease with fluence, the chemical equilibrium has been reached. The sputtering yield used in Equation A.2 is indicated near the top axis. Further details are described in the text.

Appendix B: Chemical equilibrium fluence

For estimating the fluence at which the sample reaches the equilibrium, the derivative of the function N(F) is calculated. We considered that the sample reaches the equilibrium when dN/dF ≤ 10^{-5} molecules per eV. This value is adopted because at this production/destruction rate, a variation of 10^{17} cm^{-2} in the column density of a molecular species i in the sample (ΔN_i) happens after fluences on the order of 10^{17} ions cm^{-2} for keV ions irradiation and 10^{16} for MeV ions irradiation (considering that $\Delta N \leq 10^{-5} \Delta F$). To obtain smaller changes in the column density of a given species (smaller ΔN_i), at these small production/destruction rates, longer irradiation fluences would be necessary. At these conditions, we consider that the sample is in equilibrium. Figure 8 illustrates the derivatives of N(F) for the parents and daughter species (including the unknown

species) in the different experiments as well as the fluence at which the sample reaches the equilibrium.

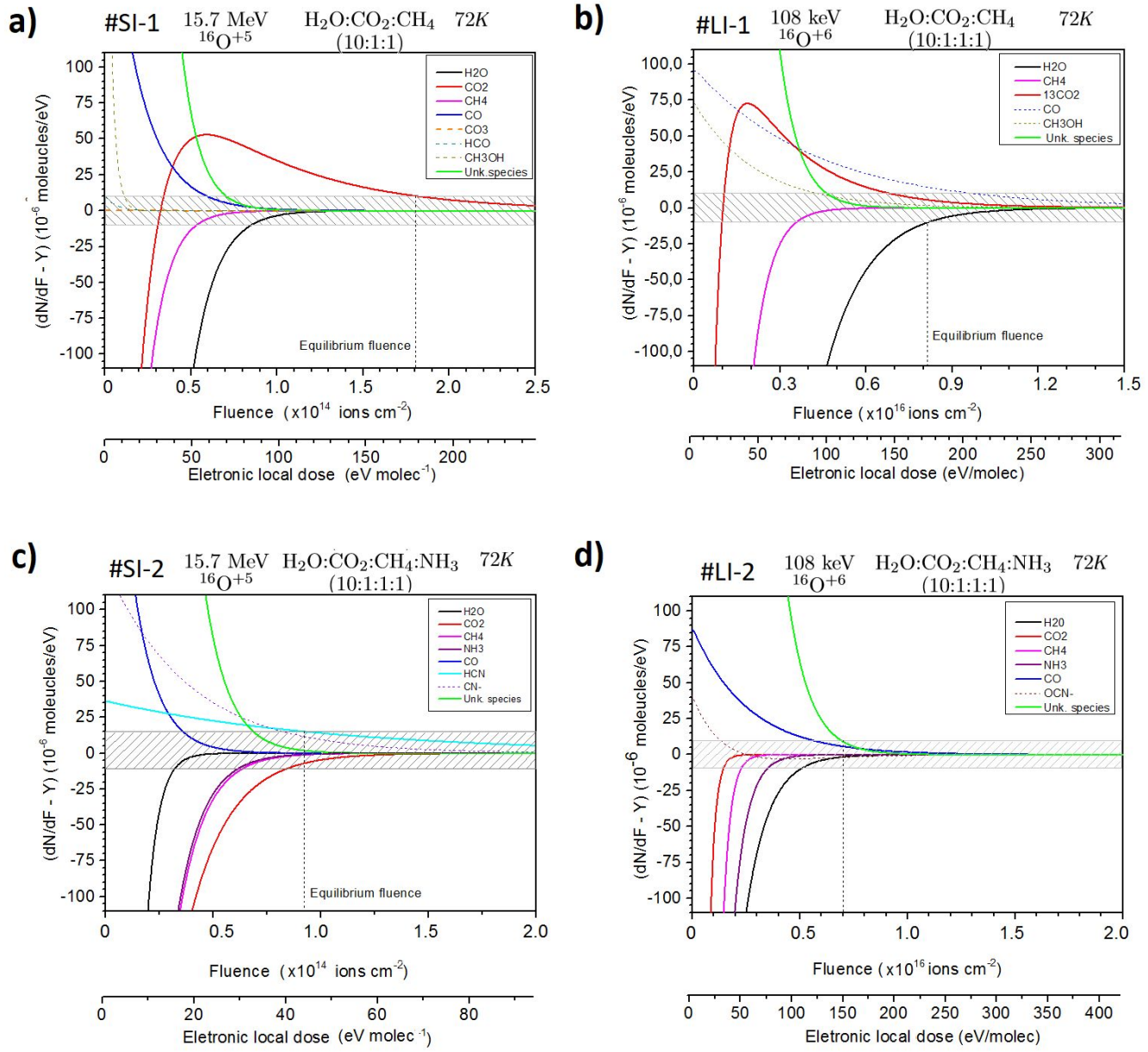

Figure B.1 – Derivative of the column density of parent, daughter and unknown species as a function of the fluence (dN/dF). The dashed line indicates the point at which the criteria for chemical equilibrium adopted here is reached (dN/dF = 10^{-5} molecules per eV). The panels show the data for: a) Experiment #SI-1; b) Experiment #SI-2; c) Experiment #LI-1 and d) Experiment #LI-2. See details in the text.